

5-Fluorouracil loaded magnetic cellulose bionanocomposites for potential colorectal cancer treatment

Mostafa Yusefi^a, Michiele Soon Lee-Kiun^b, Kamyar Shameli^{a,*}, Sin-Yeang Teow^{b,*},
Roshafima Rasit Ali^a, Kit-Kim Siew^c, Hui-Yin Chan^b, Magdelyn Mei-Theng Wong^b,
Wei-Ling Lim^c, Kamil Kuča^{a,d}

^a Malaysia-Japan International Institute of Technology, Universiti Teknologi Malaysia, Jalan Sultan Yahya Petra, 54100 Kuala Lumpur, Malaysia

^b Department of Medical Sciences, School of Medical and Life Sciences, Sunway University, Jalan Universiti, Bandar Sunway, 47500, Selangor Darul Ehsan, Malaysia

^c Department of Biological Sciences, School of Medical and Life Sciences, Sunway University, Jalan Bandar Sunway, 47500, Selangor Darul Ehsan, Malaysia

^d Faculty of Science, Department of Chemistry, University of Hradec Kralove, Hradec Kralove, Czech Republic

ARTICLE INFO

Keywords:

Cellulose
Fe₃O₄-nanoparticles
Composites
5-Fluorouracil
Drug carrier system
Colorectal cancer
Microfluidic
Co-culture

ABSTRACT

Magnetic polymer nanocomposites are inherently multifunctional and harbor assorted physiochemical actions for applications thereof as novel drug nanocarriers. Herein, Fe₃O₄-nanoparticles were supported on rice straw cellulose for 5-fluorouracil carrier abbreviated as MC/5-FU for potential colorectal cancer treatments. Several analyses indicated the multifunctional properties of MC/5-FU bionanocomposites. Transmission and scanning electron microscopy study demonstrated that Fe₃O₄ nanofillers covered the cellulose matrix. The drug release from MC/5-FU was evaluated under various pH and temperature conditions, showing the maximum release at pH 7.4 and 44.2 °C. In *in vitro* anticancer assay, MC/5-FU exhibited enhanced selectivity and anticancer actions against 2D monolayer and 3D tumour spheroid models colorectal cancer cells. The anticancer effects of MC/5-FU with magnetic targeting and heat induction were also examined. This easily synthesized MC/5-FU indicated the potential in application as a low-cost drug formulation for colorectal cancer treatments.

1. Introduction

Cellulose is a vital component of the plant cell wall and the most abundant biopolymer on earth with a “green fate” manner (Sun et al., 2019). In this respect, the off-field use of rice straw as the second-highest agro waste is intriguing since it contains approximately 45% cellulose (Yusefi, Bte Rasit Ali, Abdullah, & Shameli, 2020). Cellulose can be isolated from wood-based resources by various methods such as bleaching and delignification to eliminate the amorphous regions and liberate the crystal regions. In addition, cellulose has been treated by for example esterification, etherification, de-polymerization, and alkali treatments to obtain significant surface functional groups, ability to bind with various drugs and metal nanoparticles (NPs), great swelling property, pH gradient, and well biocompatibility (Sun et al., 2019; Yusefi & Shameli, 2021). Hence, cellulose and cellulose-based composites are finding their applications in drug delivery systems.

As a chemotherapy medication, 5-fluorouracil (5-FU) has been widely used to treat colorectal cancer for over six decades. However, it

may cause the harmful side effects due to for example high-dose chemotherapy, non-specific targeting, and lack of bioavailability (Nasri, Ebrahimi-Hosseinzadeh, Rahaie, Hatamian-Zarmi, & Sahraeian, 2020). Polymer-based drug delivery systems can decrease the above issues through affecting the microenvironment of tumors, which is leaky with a higher sensitivity to macromolecules than healthy cells (Bae & Park, 2015). For example, compared to 5-FU alone, magnetic nanotheranostics coated with polyethylene glycol/5-FU/layered double hydroxide caused a targeted action and higher anticancer effects against liver cancer HepG2 cells and lower toxicity against the healthy fibroblast 3T3 cells (Ebadi, Saifullah, Buskaran, Hussein, & Fakurazi, 2019). Being as a pH-sensitive carrier, biodegradable, and possessing the enzymatic degradation by colonic microbial agents, polysaccharides such as natural cellulose have triggered probes for novel polymeric-anticancer drug conjugates with antiproliferative actions (Sun et al., 2019; Tan, Lee, Dabdawb, & Abd Hamid, 2019). Although has obtained success in some cases, cellulose-based single-modality chemotherapies with pH-sensitive carrier structure may not be externally guided for the multi-

* Corresponding authors.

E-mail addresses: kamyarshameli@gmail.com (K. Shameli), ronaltdt@sunway.edu.my (S.-Y. Teow).

<https://doi.org/10.1016/j.carbpol.2021.118523>

Received 2 December 2020; Received in revised form 20 July 2021; Accepted 1 August 2021

Available online 4 August 2021

0144-8617/© 2021 Elsevier Ltd. All rights reserved.

stage drug release procedures. Further, several hours are required to obtain the action of pH-sensitive cellulose in human body. Thus, there is still dose limitation and unmet requirements for the multi-stimuli responsive release of drug from cellulose alone in carrier systems.

Magnetic cellulose composites are attractive candidates for remote controllability and noninvasive heat generation in cancer therapy (Liao & Huang, 2020). Cellulose as solid supports is able to assemble clusters of magnetic NPs inclusions to enhance multi-functionality and biodegradability of the magnetic complex. In turn, the functional groups of magnetic nanofillers (such as Fe₃O₄-NPs) offer exogenous groups and magnetic property for cellulose (Nypelö, Rodriguez-Abreu, Rivas, Dickey, & Rojas, 2014). Cellulose may show interactions with the NPs such as Van der Waals and H-bonding interactions to obtain magnetic responsive cellulose complex (Strassburg, Mayer, & Scheibel, 2020). Magnetic cellulose composites can be synthesized via two methods of *ex situ* and *in situ* (Pineda, Quintana, Herrera, & Sánchez, 2020). The *ex situ* or lumen loading method is a two-step process based on the physical deposition of Fe₃O₄-NPs onto cellulose. Whereas, the *in situ* synthesis is a one-step procedure using both physical and chemical reactions for the simultaneous synthesis and loading of the NPs onto cellulose (Liao & Huang, 2020).

Compared to the individual Fe₃O₄-NPs, delivering the clusters of the magnetic NPs onto malignant tumors may improve the temperature-responsive structure, owing to the inter-particle interaction with one another to enhance the magnetic field (Evans, Bausch, Sienerth, & Davern, 2018). Therefore, the development of magnetic cellulose composites as smart pH and thermo-sensitive carriers with multifunctional components, merging various modalities, has gained attention owing to their potential synergistic impacts on combination therapy (Liao & Huang, 2020). In particular, besides the pH-response, a noninvasive and low-cost method of heat induction could trigger additional driving force to obtain the sustainable drug release from magnetic cellulose composites for multimodality treatment of cancer. Previous studies have used external stimuli such as heat induction for possible treatments of H1299 lung cancer (Pawlik et al., 2013) and bone cells (cellosaurus cell line MLO-Y4) (Dolan, Haugh, Voisin, Tallon, & McNamara, 2015). In a different study, magnetic alginate-chitosan microspheres was served as a doxorubicin carrier, that the heat induction controlled the drug release from the microspheres to improve potential killing effects against MCF-7 breast cancer cells (Xue et al., 2018).

To the best of our knowledge, this is the first time that rice straw cellulose matrix was merged with Fe₃O₄ nanofillers to fabricate magnetic cellulose bionanocomposites as a 5-FU carrier to evaluate its pH- and thermal-response in drug release and then potential colorectal cancer effects *in vitro*. A series of analyses examined the structural, morphological, and thermal characteristics of the synthesized materials. The stimuli-responsive 5-FU release from the fabricated bionanocomposites was evaluated in media at different pHs and heat induction. The anticancer activities of the synthesized samples were evaluated against HCT116 and HT29 3D tumour spheroid models with magnetic targeting and heat induction. In addition, caspase assay and mitochondrial membrane potential assay were performed to evaluate the potential killing mechanisms of bionanocomposites, whereas, hemolysis assay was carried out to assess the biocompatibility of the samples.

2. Materials and methods

2.1. Chemicals and materials

Rice straw (RS) was collected from Malaysian Institute of Agricultural Research and Development (MARDI). KOH (85%, EM Science), NaClO₂ (80%, Fluka), CH₃COOH, FeCl₂·4H₂O (99%), FeCl₃·6H₂O (97%), and NaOH (99.0%) were all purchased from Sigma-Aldrich (St Louis, MO, USA). 5-FU (99%), with a molecular weight of 130.08 g·mol⁻¹ was purchased from ACROS Organics, New Jersey, USA.

2.2. Isolation of cellulose fibers from rice straw waste

The rice straw waste powder (30 g) was dewaxed by using a soxhlet instrument containing 450 mL solution of toluene/ethanol 2:1 (v/v) for 12 h at 70 °C. The sample was washed with distilled water three times and mixed with sodium chloride solution (1.4%), followed by dropwise addition of acetic acid to adjust the pH to around 4 at 70 °C under 100 rpm magnetic stirring for 5 h. The sample was washed three times and then treated with KOH solution (5%) for 12 h, and the procedure was quenched by ice water bath (2 °C) into the sample solution. The aqueous sample was centrifuged at 12,000 rpm and then freeze-dried (Free-Zone 1.0 L Benchtop Freeze Dry System) at -30 °C for 24 h to obtain the white pulpy fiber sample and termed as cellulose hereafter.

2.3. Preparation of magnetic cellulose bionanocomposites

Bionanocomposites of magnetic cellulose (MC) was prepared by a facile and one-step co-precipitation method (Pineda, Quintana, Herrera, & Sánchez, 2020; Yusefi, Shameli, Ali, Pang, & Teow, 2020). The isolated cellulose (0.05 g) was dissolved in 40 mL of distilled water at room temperature under 300 rpm magnetic stirring for 15 min. Then, FeCl₃·6H₂O and FeCl₂·4H₂O (1:2 molar ratio) were added into the cellulose solution and stirred for 45 min. After that, adding sodium hydroxide to the solution adjusted the pH around 11 under magnetic stirring for another 30 min at 25 °C to fabricate Fe₃O₄-NPs onto the cellulose network. The solution was neutralized through washing and centrifuged three times at 7000 rpm for 12 min. The suspended sample was freeze-dried at -30 °C for 24 h and termed as MC.

2.4. 5-Fluorouracil loading into magnetic cellulose bionanocomposites

The drug loading procedure was performed as 50 mg MC and 5 mg 5-FU were mixed in 250 mL distilled water solution for 14 h at continuous magnetic stirring (200 rpm) (Yusefi et al., 2020). Then, the drug-loaded sample was centrifuged at 4000 rpm for 8 min. The supernatant was analyzed using UV-Vis spectrophotometry (UV-1600, Shimadzu, Japan) at λ_{max} = 266 nm to determine the amount of the untrapped 5-FU drug. The collected sample was freeze-dried at -30 °C for 24 h and termed as MC/5-FU. The amount of drug-loaded in MC/5-FU was determined by using a calibration curve generated from known concentrations of 5-FU to calculate percentage of loading capacity (LC) and encapsulation efficiency (EE) according to Eq. (1) and (2), respectively.

$$LC (\%) = \frac{(\text{Initial drug amount in formulation (mg)} - \text{Untrapped drug (mg)})}{\text{Total weight of MCF/5FU}} \times 100 \quad (1)$$

$$EE (\%) = \frac{(\text{Initial drug amount in formulation (mg)} - \text{Untrapped drug (mg)})}{\text{Initial drug amount in formulation (mg)}} \times 100 \quad (2)$$

2.5. *In vitro* release of 5-fluorouracil

UV-Visible spectrophotometry (UV-1600, Shimadzu, Japan) was used to evaluate drug release from MC/5-FU. The UV absorbance of 5-FU at five different concentrations (1.0–5.0 $\mu\text{g}\cdot\text{mL}^{-1}$) was measured in a glass cuvette of 1.0 cm width at $\lambda_{\text{max}} = 266$ nm. The release of 5-FU from MC was studied by using a 5 mL dialysis bag (molecular weight cut-off between 12,000 and 14,000 Da). Before the experiment, the bag was soaked for 12 h in the release media of the simulated colorectal fluid (phosphate-buffered saline (PBS) of pH 7.4). Then, the solution mixture of 5 mg MC/5-FU and 2 mL release media was suspended in the 5 mL dialysis bag with the two ends tied. The bag was respectively immersed into three different release media (40 mL) maintained at 34.2, 37, and 44.2 °C at 100 rpm on a rotary shaker. 1 mL aliquot withdrawn from the system at the selected time. The collected sample at a different time point was characterized spectrophotometrically. The same study was performed in hydrochloric acid (HCl) solution at pH 1.2. The results obtained from the media with different pH values and temperatures were calculated by the following Eq. (3):

$$\text{Drug release (\%)} = \frac{\text{The amount of drug released at time 't'}}{\text{The total amount of drug loaded onto the sample}} \times 100 \quad (3)$$

All experiments were carried out in triplicate and the data were expressed as mean \pm standard deviation.

2.6. Characterization

The structural characteristics of the samples were analyzed by using PANalytical X'Pert PRO X-ray diffractometer (XRD) with the wavelength Cu K α radiation ($\lambda = 0.15406$ nm). An applied current of 20 mA and accelerating voltage of 45 kV in the range of $2\theta = 5^\circ$ – 80° with the scanning rate = $2\theta\cdot\text{min}^{-1}$ were fixed. Results from XRD were analyzed and transferred to a pattern through PAN analytical X'pert PRO software (Philips, Netherlands). The chemical and super-molecular structural analysis was determined by Fourier transform infrared spectroscopy (FTIR) spectroscopy (Thermo Nicolet, USA) under ambient conditions. First, the sample was crushed with KBr at a ratio of 1:100 (w/w) and compressed into a transparent pellet. The spectra was evaluated at the transmittance mode in a range between 4000 and 400 cm^{-1} with a 4 cm^{-1} resolution and an accumulation of 128 scans. X-ray photoelectron spectroscopy (XPS) was conducted using a Thermo Scientific, ESCALAB 250Xi Mg X-ray resource. The incidence angle of the monochrome Al K α radiation (1 mm^2 irradiation area, $300 \times 700\ \mu\text{m}$ analyzed area) was set to 54.4° and the photoelectron emission angle was $\alpha_{\text{out}} = 0^\circ$, with respect to the surface normal. The hemispherical electron energy analyzer operated in the constant analyzer energy mode at an analyzer pass energy of $E_p = 80\text{ eV}$ (survey spectra) and $E_p = 10\text{ eV}$ (high-resolution detailed spectra). The component contents in MC/5-FU were estimated by Inductively Coupled Plasma (ICP) Optical Emission Spectrometer (OES) on a VARIAN VISTA-PRO and CasaXPS software. Scanning electron microscopy (SEM) instrument (model JSM 7600F SEM) presented images of SEM to analyze the morphology and particle size of the samples. Low-acceleration voltage (10 kV) prevented the degradation of the samples. Transmission electron microscopy (TEM) (Model

JEM-2100F, Japan) was used to determine the morphology, particle size, and structure of the samples, along with the attached energy-dispersive X-ray spectroscopy (EDX) to study the elemental compositions. The synthesized bionanocomposites was evaluated through vibrating sample magnetometer (VSM) (Model 7400, Tokyo, Japan) to provide the magnetic properties of the sample at an ambient condition. Thermal analysis was carried out by using thermogravimetric analysis (TGA) (STA F3 Jupiter) Q50 V20 with a $10^\circ\text{C}/\text{min}$ heating rate under a nitrogen atmosphere (10 mL/min) at temperatures from 10°C to 800°C . Dynamic light scattering (DLS) was used to evaluate the average zeta potential value and hydrodynamic diameter of the samples, using Anton Paar instruments (LitesizerTM 500 and SurPASSTM 3) as the samples were diluted with distilled water at 5% v/v concentration. For the swelling analysis of MC/5-FU, the sample was separately immersed in solutions of PBS at pH 7.4 and HCl at pH 1.2 with various temperature inductions at 34.2, 37, and 44.2°C on a rotary shaker at 100 rpm. At each interval, the sample was collected from the solution and blotted on a filter paper to eliminate excess water and it was immediately weighed to determine the weight of the wet sample. The swelling ratio of MC/5-FU was determined as W_t/W_0 , in which W_t and W_0 are the obtained wet weights at the arbitrary and initial time, respectively.

2.7. Cell lines and reagents

HCT116 (ATCC CCL-247), HT29 (ATCC HTB-38) colorectal cancer cell lines, and CCD112 colon normal cell lines (ATCC CRL-1541) were purchased from ATCC and cultured according to ATCC's recommendation (Yusefi et al., 2021a). HCT116 and CCD112 cell lines were maintained in Dulbecco's Modified Eagle's medium (DMEM) supplemented with 10% fetal bovine serum (FBS) and GibcoTM Penicillin-Streptomycin ($100\text{ U}\cdot\text{mL}^{-1}$), while HT29 was maintained in RPMI1640 medium supplemented with 10% fetal bovine serum (FBS) and GibcoTM Penicillin-Streptomycin ($100\text{ U}\cdot\text{mL}^{-1}$).

2.8. Luminescence based *in vitro* cytotoxicity assays in 2D and 3D culture

To determine the cellular killing effect from the MC and MC/5-FU samples, cytotoxicity assays were performed using a CellTiter-Glo 2.0 Luminescent Cell Viability Assay (#G9241, Promega) on 2D monolayer models and CellTiter-Glo 3D Cell Viability Assay (#G9681, Promega) on 3D tumour spheroid models, respectively, according to the manufacturer's instruction with slight modifications as previously described (Teow et al., 2019; Yew et al., 2019). Briefly, 5000 cells per well ($100\ \mu\text{L}/\text{well}$) were seeded into a white 96-well plate and incubated overnight at 37°C in a 5% CO_2 , 95% humidified incubator (Heracell VIOS 160i, Thermo Fisher Scientific). For tumour spheroid formation, cells were seeded onto CellCarrier Spheroid ULA 96-well plate (#6055330, Perkin Elmer) and incubated for 48 h before the treatment. Dried powders of MC and MC/5-FU were weighed and prepared in the stock concentrations of $5\text{ mg}\cdot\text{mL}^{-1}$, while the 5-FU powder was prepared in $1\text{ mg}\cdot\text{mL}^{-1}$. 2-Fold serially diluted 5-FU samples (0, 7.81, 15.62, 31.25, 62.53, 125, 250, and $500\ \mu\text{g}\cdot\text{mL}^{-1}$) and MC or MC/5-FU (0, 39, 78.1, 156.3, 312.5, 625, 1250 and $2500\ \mu\text{g}\cdot\text{mL}^{-1}$) in $100\ \mu\text{L}$ per well were added and the plate was incubated for 72 h at 37°C in the 5% CO_2 incubator. Then, $100\ \mu\text{L}$ of reagent per well was added into the plate and incubated for an

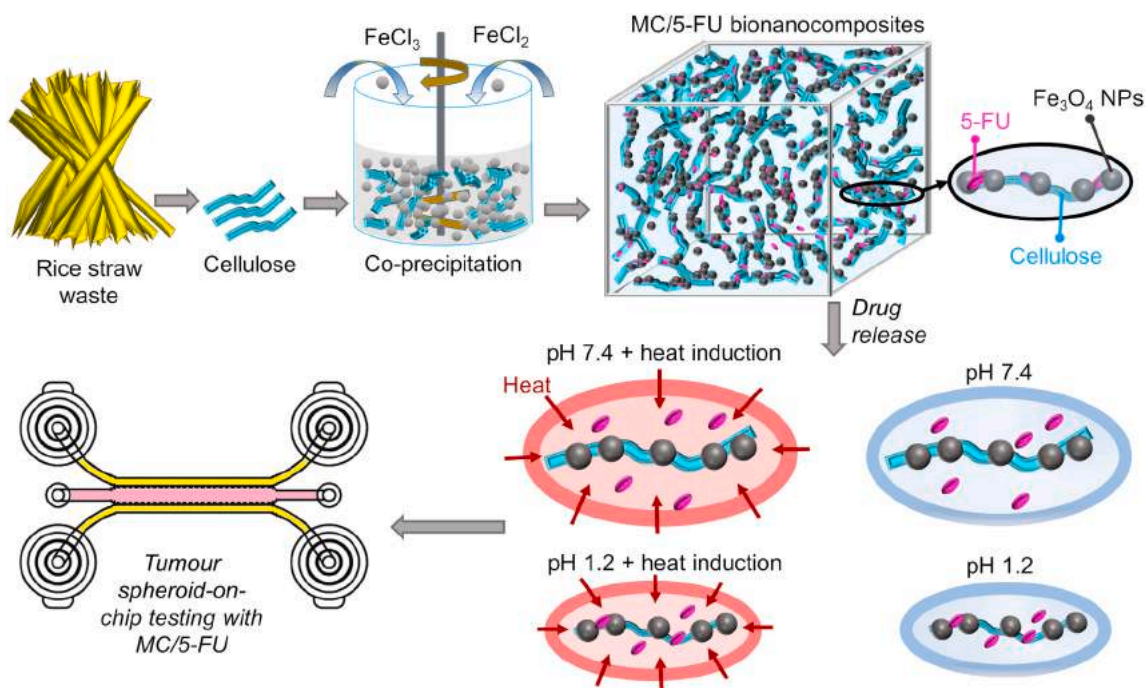


Fig. 1. The schematic processes of MC/5-FU preparation for elimination of colorectal cancer cells.

additional 1 h at 37 °C in the 5% CO₂ incubator for plate reading using a multimode microplate reader (Tecan). The dose-response graph was plotted by calculating the percent cell viability using Eq. (4):

$$\% \text{Cell viability} = \frac{\text{Relative luminescence unit (RLU) of sample well (mean)}}{\text{Relative luminescence unit (RLU) of control well (mean)}} \times 100 \quad (4)$$

In addition, the inhibitory concentration causing 50% growth inhibition (IC₅₀) was determined using an online calculator (<https://www.aatbio.com/tools/ic50-calculator>) as previously described (Ismail et al., 2019; Sukri et al., 2019). Selectivity index (SI) was also calculated using Eq. (5) to determine the selectivity of the samples towards the cancerous cells.

$$\text{Selectivity index (SI)} = \frac{\text{IC}_{50} \text{ of compound on CCD112 normal cells}}{\text{IC}_{50} \text{ of compound on HCT116/HT29 cancer cells}} \quad (5)$$

Three independent experiments were carried out, and the data were expressed as mean ± standard deviation for all triplicates within an individual experiment.

2.9. Caspase assay

To evaluate whether MC/5-FU induced apoptosis in the treated cells, caspase assay was carried out using the Chemicon *in situ* FLICA Pan-Caspase detection kit (#APT400, Merck), according to the manufacturer's instruction. HCT116 and HT29 colorectal cancer cell lines were treated with 100 and 90 μg·mL⁻¹ MC/5-FU, respectively, for 24 h and the caspase activity was measured using a multimode microplate reader (Tecan) (Excitation/emission — 490/520 nm) for rhodamine and 485/535 nm for fluorescein isothiocyanate (FITC) and fluorescence microscopy. The samples were observed under an inverted fluorescence microscope (Nikon Eclipse Ti-S, Japan) and images were captured using the Nikon NIS-Elements (Japan) microscope imaging software at a magnification of 20×.

2.10. Mitochondrial membrane potential (JC-1) assay

Cell vitality status were evaluated by examining the cellular mitochondrial function using JC-1 mitochondrial membrane potential assay Kit (#10009172, Cayman Chemical, MI, USA) following the manufacturer's instruction as previously described (Lee et al., 2019). HCT116 and HT29 cells were treated with 100 and 90 μg·mL⁻¹ MC/5-FU, respectively, for 24 h and the mitochondrial behavior was assessed through JC-1 staining. In healthy cells, JC-1 forms complexes and form aggregates in red fluorescence meanwhile unhealthy cells exhibit green fluorescence. The health status of cells were measured using a multimode microplate reader (Tecan) (excitation/emission — 535/595 nm for rhodamine and 485/535 nm for FITC) and fluorescence microscopy. The samples were observed under an inverted fluorescence microscope (Nikon Eclipse Ti-S, Japan) and images were captured using the Nikon NIS-Elements (Japan) microscope imaging software. The ratio of fluorescence intensity of rhodamine (healthy cells) and FITC (unhealthy cells) was determined and plotted. FITC (diffuse green J-monomers) indicates the unhealthy status, and rhodamine (red mitochondrial J-aggregates) indicates the healthy status. Images were captured at magnification of 20×.

2.11. Hemolysis assay

The hemolysis assay was carried out as previously described with slight modifications (Teow & Atif Ali, 2016; Yew et al., 2019). As the synthesized MC/5-FU can be potentially used in parenteral administration, blood from a healthy volunteer was diluted with 1× PBS. 100 μL of diluted blood was added into each tube with various concentrations of MC and MC/5-FU (125, 250, 500, 1000 and 2000 μg·mL⁻¹) in 400 μL. Equal volume of PBS and polyethyleneglycol (PEG) were used as blank and negative controls, respectively. 0.5% Triton X-100 was used as positive control. Separate sets of MC and MC/5-FU at similar concentrations without addition of blood were also prepared to account for the background colours. All tubes were incubated at 37 °C in a 5% CO₂ and 95% humidified incubator for 3 h. The tubes were then centrifuged at 800 ×g for 15 min. 100 μL supernatant was transferred to a 96-well plate in triplicates and read at OD 540 nm using the multimode microplate

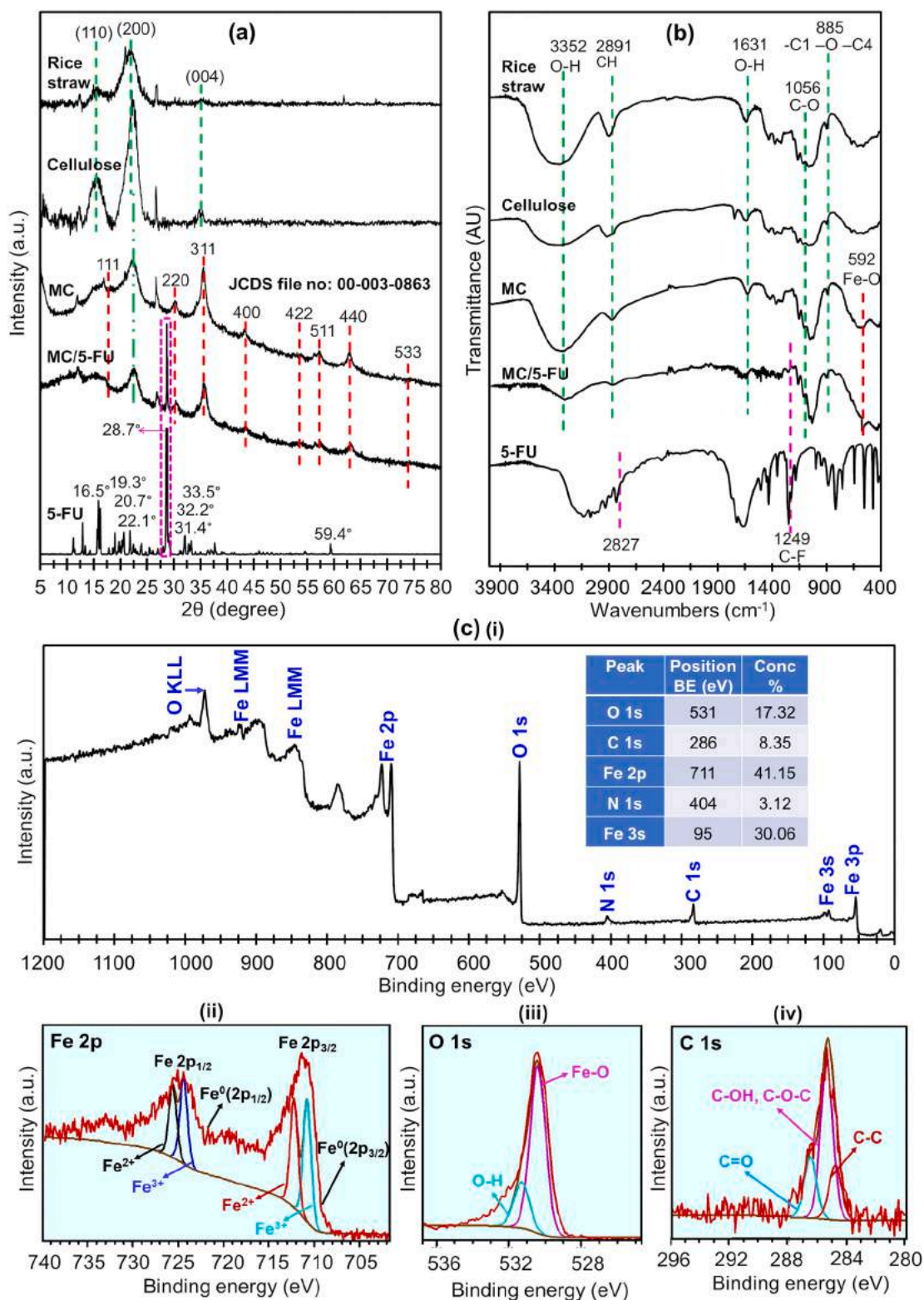


Fig. 2. (a) XRD and (b) FTIR spectroscopy of rice straw waste, cellulose, MC, MC/5-FU, and 5-FU. (c) XPS analysis of MC/5-FU, (i) wide scan, (ii) Fe 2p, (iii) O 1s, and (iv) C 1s.

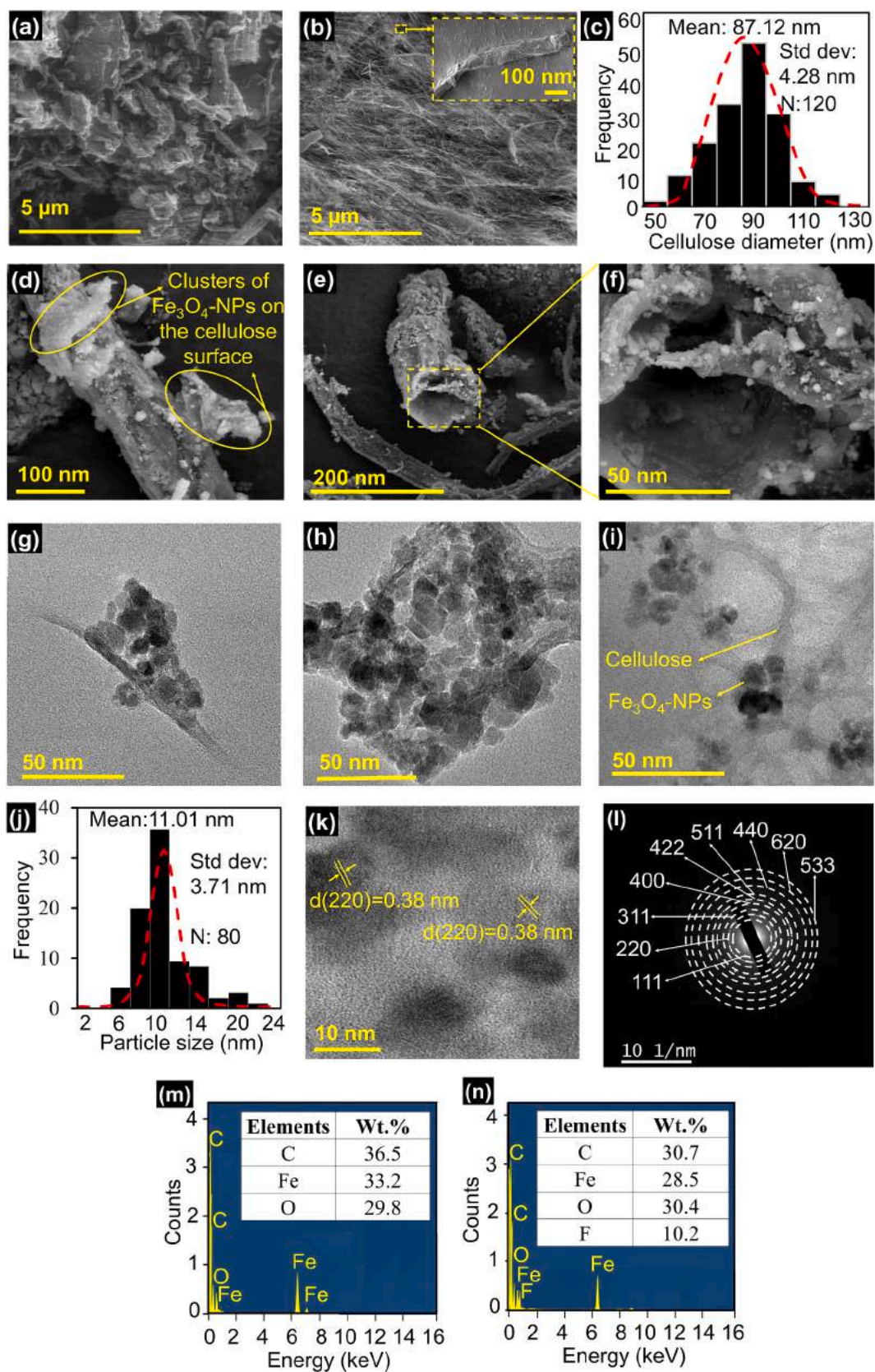


Fig. 3. SEM image of (a) dewaxed rice straw waste and (b) cellulose. (c) Histogram of cellulose diameter distribution. SEM images of (d) MC and (e, f) MC/5-FU. (g–i) TEM images, (j) histogram of Fe₃O₄-NPs size distribution, (k) the electron diffraction pattern, and (l) SAED pattern of MC/5-FU. (m) EDX of MC and (n) MC/5-FU.

reader (Tecan). A standard curve was plotted by measuring the OD of diluted supernatant of Triton X-100 hemolysed blood (0, 3.13, 6.25, 12.5, 25, 50 and 100%). The percent hemolysis of MC and MC/5-FU was determined using the standard curve. The OD value was subtracted by their background interference (various concentrations of the sample without blood). The data were expressed as mean \pm standard deviation for all triplicates within an individual experiment.

2.12. Tumour-on-chip experiment and magnetic targeting assay

Tumour spheroids were generated as described above, harvested and injected along with Matrigel matrix (#354234, Corning) into 3D Cell Culture Chips 3DT (Aim Biotech, Singapore) following the manufacturer's instruction. The Matrigel was left for 30 min for polymerization. Fibronectin (#610077, BD) was prepared in $5 \mu\text{g}\cdot\text{mL}^{-1}$ and used to coat both the side channel for cell adhesion. Next, human umbilical vein endothelial cells (HUVEC) (#C-12203, PromoCell) were prepared in 2×10^6 cells mL^{-1} and injected into both side channels. The chip was incubated at 37°C , 5% CO_2 overnight for complete adherence. 100 $\mu\text{g}\cdot\text{mL}^{-1}$ MC/5-FU were prepared and injected into the side channels followed by 72 h incubation for HCT116. The changes of spheroid size were monitored every 24 h and images were captured using the inverted microscope (AE2000 Motic) at magnification of $10\times$. The size of the spheroid was measured using the software and the percentage of growth was calculated and compared between the untreated control and MC/5-FU treated spheroids.

To examine the effect of anticancer killing by magnetic targeting, the co-culture model was generated as abovementioned and the MC/5-FU was directed towards the individual spheroid using an external magnet. The magnet was placed on top of the spheroid throughout the 72 h treatment of MC/5-FU. The killing effect was compared to the co-culture model with MC/5-FU treatment but without magnetic targeting. To assess the live/dead cell status of spheroid, 0.5 μM Calcein AM (#C1430, Invitrogen) and 16 $\mu\text{g}\cdot\text{mL}^{-1}$ propidium iodide (PI) (#556463, BD Pharmingen) were used to stain the HCT116 spheroids in the chip for 1 h at 37°C as described previously (Kessel et al., 2017) before viewing under the inverted fluorescence microscope (Nikon Eclipse Ti-S, Japan). Images were captured at $10\times$ magnification and overlaid using the Nikon NIS-Elements (Japan) microscope imaging software.

2.13. Short-term heat induction assay

To examine the effect of short-term heat induction on the anticancer activity of MC/5-FU, an assay was developed using a thermal cycler (SureCycler 8800, Agilent Technologies) with the 'temperature gradient' function. Tumour spheroids were generated as described above and individually transferred to sterile PCR tubes. HCT116 spheroids were treated with 100 $\mu\text{g}\cdot\text{mL}^{-1}$ MC/5-FU and transferred to the thermal cycler. The temperature gradient ranging from 34.2 to 44.2°C was initiated and incubated for 1 h. The tubes were transferred and incubated in the 37°C CO_2 incubator for additional 24 h before the anticancer killing was determined using CellTiter-Glo 3D Cell Viability Assay as described above. The immediate killing of spheroid after 1 h incubation of MC/5-FU was also measured for comparison. The data were expressed as mean \pm standard deviation for all triplicates within an individual experiment.

3. Results and discussion

Fig. 1 depicts the schematic process of this study as MC/5-FU bionanocomposites contained a complex of rice straw cellulose solid support, Fe_3O_4 -NPs as fillers, and anticancer drug 5-FU. The potential multi-stimuli responsive release of 5-FU from MC/5-FU was evaluated. Finally, the anticancer actions of MC/5-FU against various colorectal cancer cells were studied.

3.1. X-ray diffraction

Fig. 2a shows the XRD diffraction patterns of the prepared samples. The extracted cellulose exhibited the patterns with the diffraction peaks at approximately $2\theta = 15.1^\circ$, 22.4° , and 35° attributed, respectively, to the cellulose crystals of 110, 200, and 004 planes for the normal cellulose-I structure (Tibolla, Pelissari, Rodrigues, & Menegalli, 2017; Yusefi, Bte Rasit Ali, Abdullah, & Shameili, 2020). Similar to a different report (Lu & Hsieh, 2012), the treatments on rice straw possibly improved organization, alignment, and crystal interfaces in the cellulose structure. The XRD diffraction pattern of MC comprised peaks related to both cellulose and magnetite Fe_3O_4 -NPs. The peaks for Fe_3O_4 -NPs were presented at 18.74° , 30.46° , 35.61° , 43.62° , 53.16° , 57.48° , 62.88° , 71.72° , and 74.30° corresponded to the crystal planes of (111), (220), (311), (400), (422), (511), (440), (620) and (533), respectively. Of this, MC was agreed to contain Fe_3O_4 (JCPDS file no.: 00-003-0863) involved a few peaks, not $\gamma\text{-Fe}_2\text{O}_3$ (JCPDS file no.: 01-089-3850) with many peaks (Yusefi et al., 2021b). As reported by another study, the increased crystallinity of the cellulose network was observed after its magnetization with embedded Fe_3O_4 -NPs (Kadam et al., 2019). The XRD peaks of both cellulose and MC showed higher intensity than those from a different study used an *ex-situ* or lumen loading method to synthesize magnetic cellulose fibers isolated from newspaper waste (Srasri et al., 2018). The presence of the drug in MC/5-FU slightly decreased the peak intensity related to MC. While, a sharp peak at 28.7° is attributed to the presence of the drug in MC/5-FU. The XRD pattern of anticancer drug 5-FU displayed various peaks at 16.5° , 19.3° , 20.7° , 22.1° , 28.7° , 31.4° , 32.2° , 33.5° , and 59.4° , which was also obtained by a different study (Li et al., 2015). Although, in the MC/5-FU pattern, these peaks of the drug were mostly overlapped with those of its composite carrier. For example, the peak of MC at 18.74° was overlapped with that of the drug at 16.50° . The above XRD results of MC/5-FU revealed the peaks attributed to cellulose, Fe_3O_4 , and 5-FU.

3.2. Fourier transform infrared spectroscopy

Fig. 2b indicates the FTIR spectra of the samples. From the spectra of cellulose, the peaks at 760 and 491 cm^{-1} were attributed to elimination of silica (Si—O—Si stretching) (Lu & Hsieh, 2012). Further results showed that the peaks at 3352 , 2891 , and 1100 cm^{-1} might determine the stretching vibrations of —OH groups, C—H stretching, and cellulose network structure, respectively (Chen, Yu, Zhang, & Lu, 2011). The peak at 1524 cm^{-1} (such as aromatic skeletal vibrations) was possibly related to the presence of pyranose ring skeletal C—O—C bonds of cellulose. In the anomeric region ($950\text{--}700 \text{ cm}^{-1}$), the minor peak at 885 cm^{-1} in cellulose spectra represents the glycosidic —C₁—O—C₄ deformation property of the β -glycosidic bond in cellulose (Jiang & Hsieh, 2013). MC and MC/5-FU displayed the main peaks of both cellulose and Fe_3O_4 . The peaks at 2891 , 1631 , and 1056 cm^{-1} were attributed to C—H, the bending mode of O—H groups, and C—O stretching groups, respectively. In addition, the peak at around 3352 cm^{-1} indicated the stretching hydroxyl groups (O—H bonds), which was shifted for different samples (Khalid et al., 2021). The CO_2 and measuring conditions potentially caused the presence of a peak at $2300\text{--}2400 \text{ cm}^{-1}$. In MC and MC/5-FU spectra, the intensity of the Fe—O band at 592 cm^{-1} could address the synthesis of the Fe_3O_4 -NPs (Izadiyan et al., 2020). From the 5-FU spectra, the peak at 1249 cm^{-1} is related to the C—F band, which was also appeared in MC/5-FU spectra with decreased intensity. The NH stretching group in 5-FU displayed a broadband at $2827\text{--}3300 \text{ cm}^{-1}$, whereas, it was overlapped with the OH group and shifted to $2930\text{--}3600 \text{ cm}^{-1}$ in the spectrum of MC/5-FU (Anirudhan, Nima, & Divya, 2015). In summary, the FTIR results identified the chemical structures of MC/5-FU as a drug-loaded magnetic cellulose bionanocomposites.

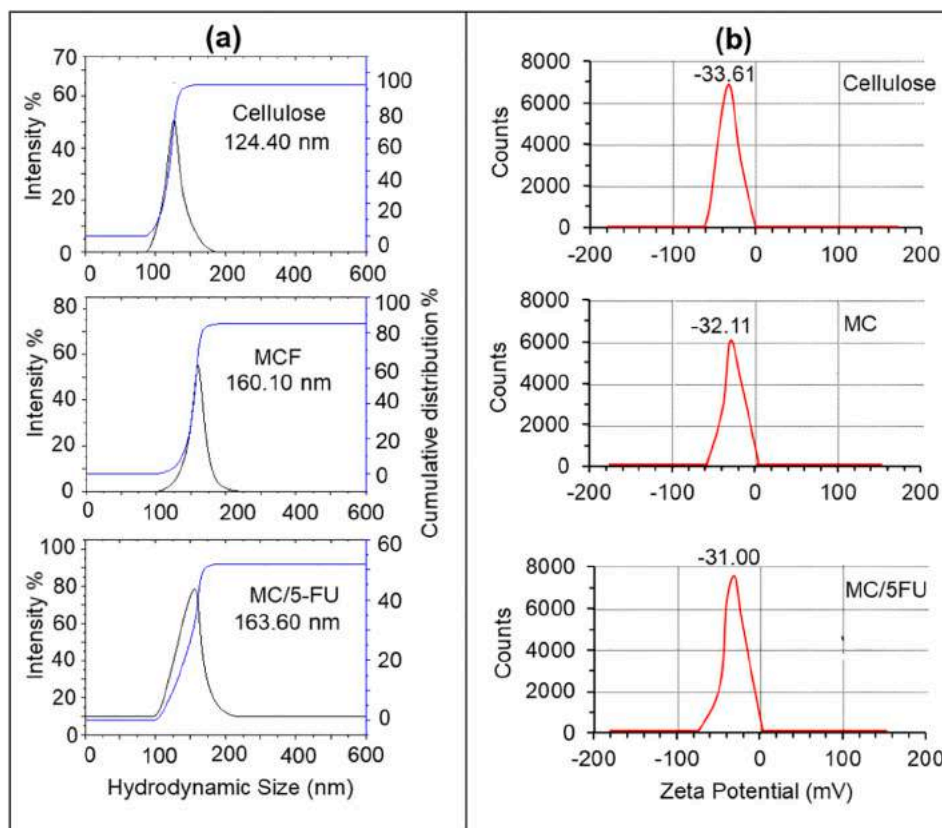


Fig. 4. (a) Hydrodynamic size and (b) zeta potential of cellulose, MC, and MC/5-FU.

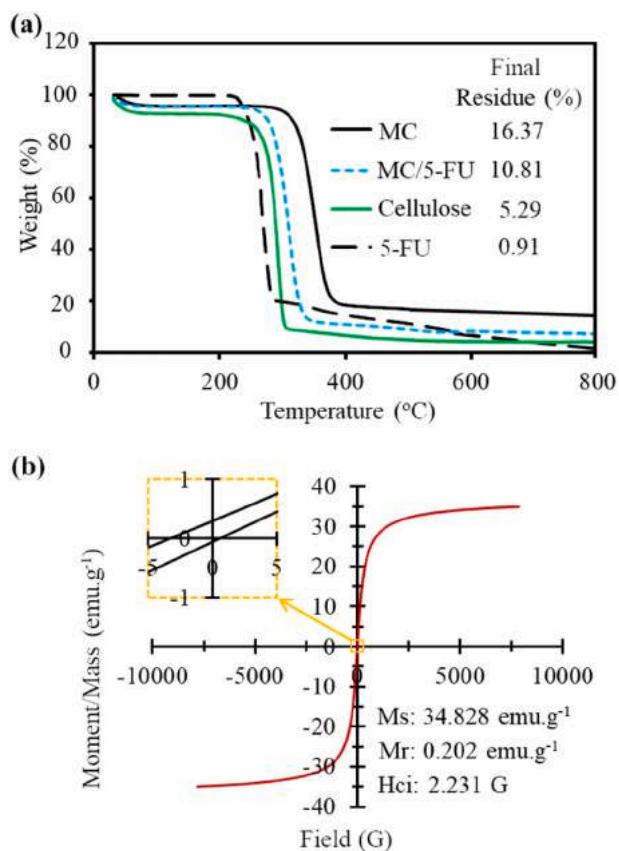


Fig. 5. (a) TGA of cellulose, MC, MC/5-FU, and 5-FU. (b) VSM of MC.

3.3. X-ray photoelectron spectroscopy

The XPS analysis examined the surface chemical composition and the bonding environment of MC/5-FU (Fig. 2c). The wide-scan XPS spectrum of the MC/5-FU (Fig. 2ci) indicates that the photoelectron lines at binding energies of about 286, 401, 404, 531, and 710 eV are assigned to C 1s, (8.35%), N 1s (3.12%), O 1s (17.32%), Fe 2p (41.15%), and Fe 3s (30.06%), respectively. The expanded peaks appearing in the Fe 2p spectrum (Fig. 2cii) are fitted with spin-orbit doublets of Fe 2p_{3/2} (711.45 eV) and Fe 2p_{1/2} (724.79 eV) as the feature peaks of Fe⁰ (Lesiak et al., 2019; Wang et al., 2016). Further, the doubles are characteristics of the peaks for Fe²⁺ and Fe³⁺, which is in an agreement with the stated values of Fe₃O₄ (Lu et al., 2019; Wang et al., 2016). The XPS spectra displays peaks with binding energy at 286 and 404 eV attributed to C 1s and N 1s, respectively. Similarly, these peaks were found by different studies on 5-FU (Todea et al., 2018) and magnetic cellulose based sample (Sabaqian, Nemat, Nahzomi, & Heravi, 2017). In the high-resolution of O 1s XPS spectra (Fig. 2ciii), the binding energy at around 529.50 and 531.50 eV were related to Fe—O and O—H bonds with area peak of 78.14 and 21.86%, respectively. These findings can possibly show that Fe₃O₄-NPs were supported on cellulose. In addition, in the C 1s core-level peak were deconvoluted into three peaks. The peaks at around 286.6, 285.2, and 284.9 eV were attributed to C=O, C—OH or C—O—C, and C—C, respectively, (Fig. 2civ). Particularly, these groups could offer several reactive sites for the bonding between Fe₃O₄ and cellulose and the mixture mostly by the presented hydroxyl groups on cellulose since the characteristic peak (286.6 eV) was the strongest peak (Q. Lu et al., 2019).

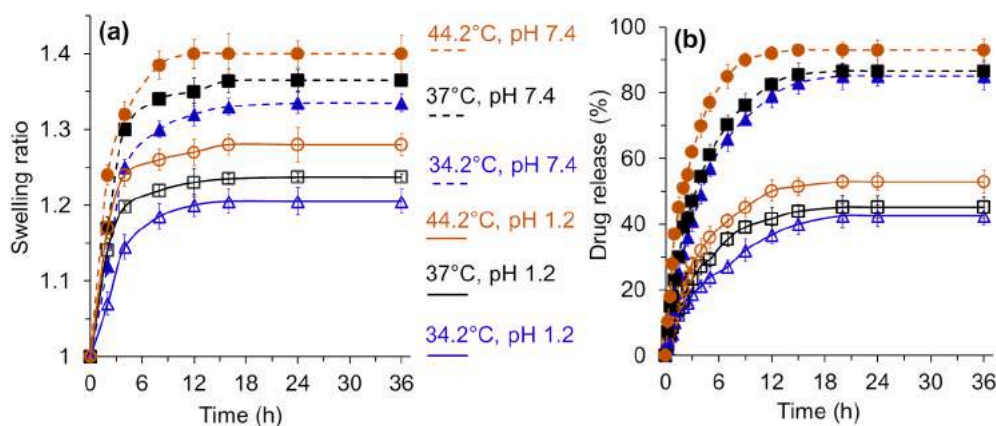


Fig. 6. (a) Swelling kinetics of MC/5-FU and (b) 5-FU release from MC/5-FU in different media at pH 1.2 and 7.4 under temperature induction from 34.2 to 44.2 °C.

3.4. Scanning electron microscopy

Fig. 3(a–n) show the results of SEM and TEM analysis of cellulose, MC, and MC/5-FU. As seen from Fig. 3(a–b), the size of the rice straw waste was gradually decreased after degradation of the hemicellulose and lignin through delignification, bleaching, and alkali treatments to liberate cellulose. The extracted cellulose was mostly in a rod-shaped structure and comprised cellulosic fibrils (Fig. 3b) with an average diameter of 87.12 ± 5.6 nm (Fig. 3c). Cellulose did not indicate magnetic particles, whereas, MC (Fig. 3d) and MC/5-FU (Fig. 3e, f) bionanocomposites showed that the clusters of Fe_3O_4 nanofillers as white-dot were distributed and attached on the cellulose solid support. In addition, loading 5-FU onto MC did not change the morphological feature of the bionanocomposites.

3.5. Transmission electron microscopy and energy-dispersive X-ray spectroscopy

The TEM images of MC/5-FU (Fig. 3g–i) showed the cellulose matrix is covered with the intercalated Fe_3O_4 -NPs. From Fig. 3g, clusters of Fe_3O_4 -NPs were supported on cellulose. Fig. 3j indicates the histogram of Fe_3O_4 -NPs size distribution as plotted from the TEM images with the mean size of 11.01 ± 2 nm. The electron diffraction pattern of MC/5-FU (Fig. 3k) shows a regular and uniform crystallinity with lattice spacing on the TEM image around 0.38 nm. From the selected area electron diffraction (SAED) pattern (Fig. 3l), diffraction rings of the Fe_3O_4 phase were indexed as (111), (220), (311), (400), (422), (511), (440), (620), and (533), which was in good agreement with the obtained XRD results. It can be understood from the EDX results that the treatments on rice straw waste dissolved silica into aqueous ions, which was subsequently replaced by carbon (Basta, Fierro, El-Saied, & Celzard, 2009). EDX of MC/5-FU (Fig. 3n) indicated the fluorine (F) element due to the presence of 5-FU, however, MC did not (Fig. 3m). The MC/5-FU contained carbon (30.7 wt%), oxygen (30.4 wt%), Fe (28.5 wt%), and fluorine (9.2 wt%). Of this, the EDX results revealed the presence of elements for MC/5-FU precursors.

3.6. Dynamic light scattering

As shown in Fig. 4a, the hydrodynamic diameter of cellulose, MC and MC/5-FU is 124.40 ± 5 , 160.10 ± 4 and 163.60 ± 2 nm, respectively. The diameter of cellulose was comparable to cellulose extracted from sugarcane bagasse fibers (Bahrami, Behzad, Zamani, Heidarian, & Nasri-Nasrabad, 2018). MC and MC/5-FU displayed bigger size than cellulose to prove the attachment of Fe_3O_4 fillers onto the cellulose matrix. From Fig. 4b, the zeta potential of cellulose, MC and MC/5-FU are -33.61 ± 2.94 , -32.11 ± 2.36 , and -31.00 ± 1.80 mV, respectively, showing a good stability of the samples in the aqueous solution. This is potentially

attributed to the electrostatic repulsion in cellulose and Fe_3O_4 -NPs (de Oliveira et al., 2017).

3.7. Thermal analysis

Fig. 5a shows the results of the thermal analysis. The initial weight loss could be related to the trapped water, which was marginally occurred in substrates of cellulose, MC, and MC/5-FU. The main weight loss of cellulose and MC were approximately at 245 and 290 °C with the final residue of 5.29 and 16.37% at 800 °C, respectively. Therefore, cellulose indicated an increase in thermal stability after its conjugation with Fe_3O_4 -NPs. From the final residue % of cellulose and MC, it can be estimated that the MC sample comprised around 12% of magnetic Fe_3O_4 -NPs. As seen in the TGA results that after 600 °C, the residues of the samples were not mainly changed. A single decomposition step at around 218 °C was found for 5-FU with the final residue of 0.91% (Gupta, Tiwari, Tiwari, Srivastava, & Rai, 2015). MC/5-FU showed the major weight loss at 261 °C with the final residue of 10.81%, which was higher than that of 5-FU alone. Hence, the thermal stability of 5-FU was enhanced after its loading onto the MC carrier.

3.8. Vibrating sample magnetometer

Fig. 5b demonstrates the magnetization loop for MC at room temperature. The VSM results of MC showed the coercivity (H_{ci}) and retentivity (M_r) of 2.231 G and $0.202 \text{ emu} \cdot \text{g}^{-1}$, respectively. Further, the saturation magnetization (M_s) value was estimated to be $34.828 \text{ emu} \cdot \text{g}^{-1}$. This reveals the successful formation of Fe_3O_4 -NPs. The cellulose matrix without the magnetic response could decrease the magnetic property of MC bionanocomposites. However, it was earlier reported that compared to individual and bare Fe_3O_4 -NPs, the same amount of the magnetic NPs in a cluster system on a matrix may desirably trigger a stronger temperature-responsive structure and magnetic properties, owing to the interparticle interactions with one another for enhancing the magnetic field (Evans, Bausch, Sienerth, & Davern, 2018).

3.9. Swelling analysis

The swelling properties of composite drug carriers might trigger a key role in the drug release behavior. Fig. 6a shows the swelling kinetics of MC/5-FU under different conditions. MC/5-FU exhibited its equilibrium state after around 12 h. It indicated maximum swelling ratios of 1.36 ± 0.011 and 1.23 ± 0.04 in the media at pH 7.4 and 1.2 at 37 °C, respectively, after 36 h. Adding the temperature and pH increased the swelling kinetics of MC/5-FU with the highest swelling ratio of 1.40 ± 0.04 in a media at pH 7.4 and 44.2 °C. As reported earlier that the cellulose based material showed higher swelling ratio at pH 7.4 than

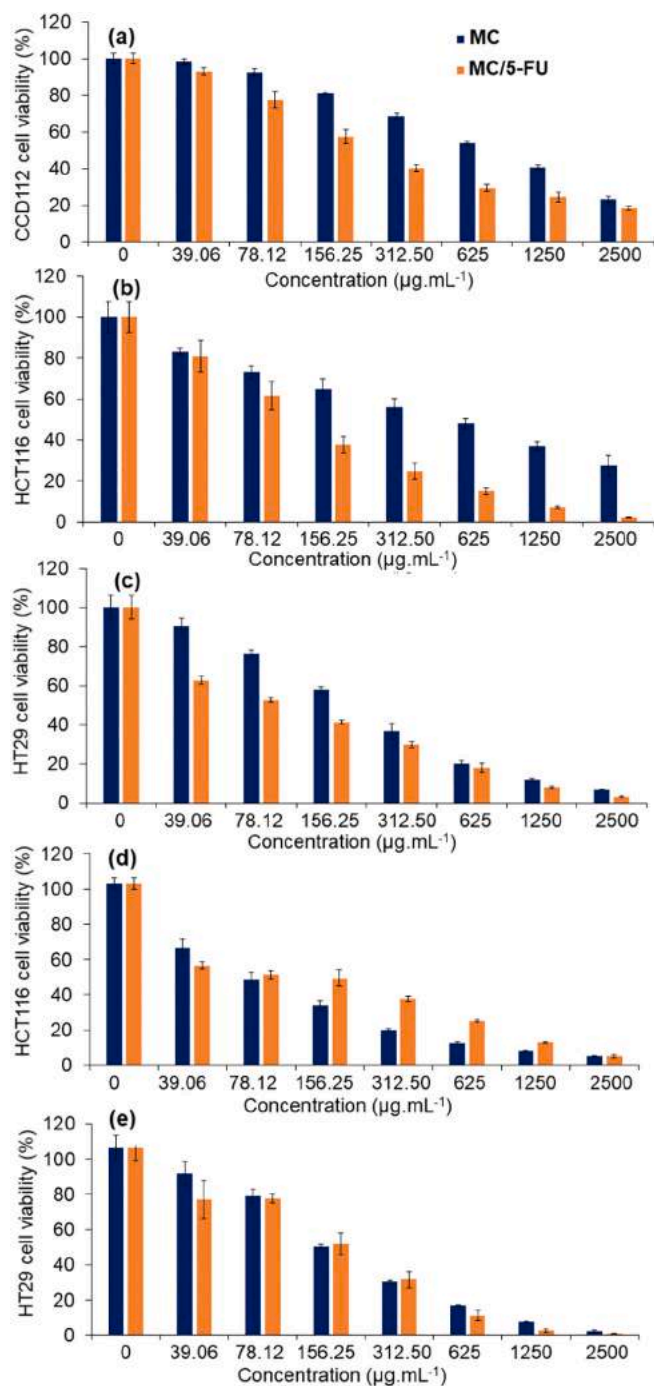


Fig. 7. Anticancer activity of MC and MC/5-FU against (a) CCD112, (b) HCT116, and (c) HT29 2D monolayer models. Anticancer activity of MC and MC/5-FU against (d) HCT116 and (e) HT29 3D tumour spheroid models.

Table 1

IC₅₀ and SI values of MC, MC/5-FU, and 5-FU in various cell lines.

Samples	CCD112 (normal) (µg.mL ⁻¹)	HCT116 (cancerous) (µg.mL ⁻¹)			HT29 (cancerous) (µg.mL ⁻¹)		
	2D monolayer	2D monolayer	3D tumour spheroid	SI _{2D}	2D monolayer	3D tumour spheroid	SI _{2D}
MC	741.79	491.28	76.10	1.51	200.61	170.92	3.70
MC/5-FU	210.73	114.58	98.60	1.84	90.85	163.24	2.32
5-FU	0.91	1.30	13.23	0.70	6.24	18.11	0.15

SI_{2D} — selectivity index of samples calculated from 2D monolayer cell lines.

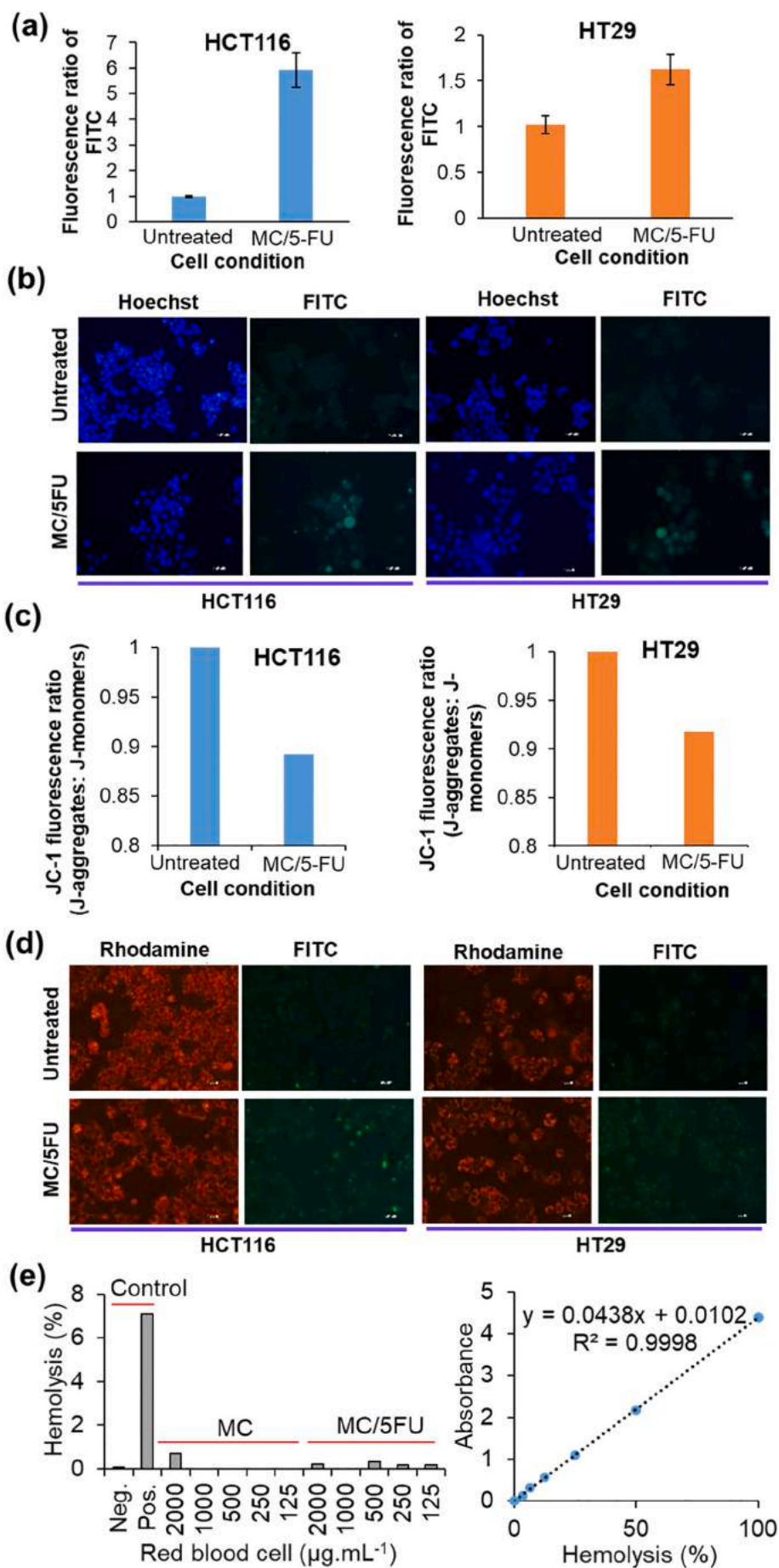
that at pH 1.2 (Bhandari et al., 2017). It can be noticed that the heat induction slightly enhanced the swelling ratio possibly due to the presence of Fe₃O₄ in MC/5-FU bionanocomposites.

3.10. Loading capacity and encapsulation efficiency

Based on the UV absorbance and Eq. (1), the LC was estimated to be $12.00 \pm 3.2\%$, indicating MC/5-FU comprised almost 12 and 88 wt% of 5-FU and MC, respectively. The EE was found to be $62.50 \pm 0.8\%$, according to the UV absorbance and Eq. (2). The alkali treatment possibly offered open bonds on the cellulose chains in which 5-FU entered into the substrate of MC (Kadry, 2019). It has been reported that loading the Fe₃O₄-NPs as fillers onto the cellulose matrix increased the crystallinity of the magnetic cellulose for potential effective bonding and release of 5-FU (Kadam et al., 2019; Seabra, Bernardes, Fávoro, Paula, & Durán, 2018). The drug could potentially have Van der Waals interaction with both cellulose and Fe₃O₄ (Doane & Burda, 2013; Li et al., 2014; Panja, Maji, Maiti, & Chattopadhyay, 2015). During the 5-FU loading procedure, the molecules of the carrier possibly become nano-gels and pliable to enhance the drug conjugation within the carrier (Zhu et al., 2013). In addition, 5-FU is a heterocyclic aromatic organic compound and has a low molecular weight to be diffused within open and expanded pores and substrate of MC (Illangakoon, Yu, Ahmad, Chatterton, & Williams, 2015).

3.11. In vitro release of 5-fluorouracil

Fig. 6b shows the release behavior of 5-FU from MC/5-FU under several conditions within 36 h. The drug release from MC/5-FU was in such a pH-responsive manner since it was almost twice higher at pH 7.4 ($86.62 \pm 3.7\%$) than that of pH 1.2 ($45.12 \pm 3.3\%$). This is possibly owing to the swelling behavior and polymer relaxation of MC/5-FU, which was also explained earlier on cellulose nanofiber aerogel loaded with bendamustine hydrochloride (Bhandari et al., 2017) and 5-FU loaded cellulose-based carrier (Anirudhan, Nima, & Divya, 2015). The drug release was investigated in media at pHs 1.2 and 7.4 under temperature induction from 34.2 to 44.2 °C. The heat induction slightly increased the initial 5-FU release from MC/5-FU. The drug release from MC/5-FU increased with increase of pH and the temperature induction, showing the highest release of $93 \pm 2.8\%$ at pH 7.4 and 44.2 °C. The mechanisms include polymer relaxation and Fickian diffusion as well as the combined procedures were frequently suggested to explain the drug release performances in such complex (Liao & Huang, 2020). In addition, the heat transfer from the temperature induction possibly improved the drug release ratio (Xue et al., 2018), indicating the positive effect of Fe₃O₄ NPs in MC composites. Several reports suggested using the heat induction as a noninvasive and inexpensive method for improvement of drug release and anticancer actions (Liao & Huang, 2020; Xue et al., 2018). The MC/5-FU formulation studied herein is possibly intriguing for further analysis on multi-stimuli responsive drug delivery systems.



(caption on next page)

Fig. 8. Caspase detection of untreated control and MC/5-FU-treated HCT116 and HT29 cells in (a) fluorescence ratio and by (b) fluorescence microscopic analysis. Mitochondrial membrane potential analysis of untreated control and MC/5-FU-treated HCT116 and HT29 cells in (c) fluorescence ratio and by (d) fluorescence microscopy. Hemolysis assay (e) of MC and MC/5-FU.

3.12. Luminescence based *in vitro* cytotoxicity assays in 2D and 3D culture

In Fig. 7(a–c), dose-dependent inhibition of MC and MC/5-FU was observed against 2D monolayer of CCD112 normal, HCT116, and HT29 colorectal cancer cells cell lines, respectively. In the three cell lines, MC/5-FU indicated potent killings based on the IC_{50} values (Table 1). To further evaluate the selectivity activity of the samples, selectivity index was calculated. As shown in Table 1, both MC (1.51 and 3.70) and MC/5-FU (1.84 and 2.32) prompted superior selectivity than 5-FU (0.70 and 0.15) for both HCT116 and HT29 cell lines. Yet, MC/5-FU as expected had higher selectivity than 5-FU alone and significantly stronger anticancer action than the unloaded MC in both HCT116 and HT29 cell lines. Although 5-FU was much potent in killing the cancer cells, the killing action was non-specific and exerted high killing in CCD112 colorectal normal cells. It is worth mentioning that 5-FU alone slightly displayed stronger action against cancer cells compared to normal cells, because it possesses prevention of the thymidylate synthetase protein enzyme to eliminate the cancer cells (Niedzwiecki et al., 2017).

To further evaluate the anticancer activities of MC and MC/5-FU, we analyzed the effects of MC and MC/5-FU using the more biologically relevant tumour spheroid models *in vitro* of HCT116 (Fig. 7d) and HT29 (Fig. 7e) cell lines. Results indicated dose-dependent killing activities of MC and MC/5-FU against the cancer cells. Interestingly, except for MC/5-FU treatment in HT29 spheroids, both MC and MC/5-FU in tumour spheroids showed improved IC_{50} values as compared to the 2D monolayer (Table 1). This suggests an effective penetration of the MC into the tumour spheroids model, which had a more complicated tissue architecture. These results revealed that the penetration profiles of the synthesized bionanocomposites are appropriate to elevate IC_{50} values in both HCT116 and HT29 spheroid models.

3.13. Caspase assay

Caspase detection assay was performed to understand the elimination mechanism of MC/5-FU. Caspase is a key enzyme in a programmed cell death process known as apoptosis; hence, the amount of caspase in the cells positively correlates with the apoptotic activity. As shown in Fig. 8a, MC/5-FU-treated HCT116 and HT29 cells presented higher ratio of FITC, as directly proportional to the amount of caspase compared to untreated control. Comparatively, higher FITC ratio was seen in the treated HCT116 cells. When fluorescence microscopy was performed, more green fluorescence was observed in the treated cells (Fig. 8b) as in line with Fig. 8a. Therefore, MC/5-FU could induce apoptosis in both HCT116 and HT29 colorectal cancer cell lines.

3.14. Mitochondrial membrane potential assay

In addition to caspase assay, the mitochondrial function of MC/5-FU-treated HCT116 and HT29 cells was examined using a commercial kit. In this assay, a cytofluorimetric cationic dye, JC-1 forms complexes known as J-aggregates with red fluorescence (rhodamine) in healthy cells, while JC-1 remains in monomeric form and exhibits green FITC in unhealthy cells. As shown in Fig. 8c, the MC/5-FU-treated cells displayed lower ratio of J-aggregates to J-monomers, indicating 0.89 and 0.92 for HCT116 and HT29, respectively. This suggested the slight impact of MC/5-FU on the mitochondrial function. This observation was also supported by the fluorescence microscopy in which MC/5-FU-treated cells displayed dimmer red J-aggregates and slightly brighter green J-monomers compared to the untreated control at a normalised background (Fig. 8d). Thus, MC/5-FU affected the mitochondrial function to

a very low extent.

3.15. Hemolysis assay

From Table 1, the IC_{50} values of MC and MC/5-FU on the three cell lines ranged from 76.1 to 741.79 $\mu\text{g}\cdot\text{mL}^{-1}$. Therefore, the hemolytic potential of samples was assessed from 125 to 2000 $\mu\text{g}\cdot\text{mL}^{-1}$. From Fig. 8e, 2000 $\mu\text{g}\cdot\text{mL}^{-1}$ of MC and MC/5-FU resulted in approximately 0.7 and 0.3% of hemolysis, respectively. The hemolysis level was expected to reduce following the decrease in concentrations. This indicates that both MC and MC/5-FU are not toxic to the red blood cells.

The above results of *in vitro* anticancer actions could prove the desirable physiochemical characteristics of MC to encapsulate 5-FU with extended dissolution and controlled release dosage. This desirably increased the mobility, binding ability, and colloidal stability of MC/5-FU in the suspension to subsequently promote its attachment onto the cancer cell surface in the 2D and 3D colorectal cancer assays (Xu et al., 2011). As a result, MC/5-FU may potentially reduce the leakage and degradation of 5-FU (Banerjee et al., 2017). MC/5-FU, therefore, may present as a potential candidate in colorectal cancer treatment.

3.16. Tumour-on-chip coculture assay

To further assess the anticancer action of MC/5-FU in a more biologically relevant model, a microfluidic chip-based co-culture model was generated. HCT-116 spheroids was grown in the middle channel of the chip in the presence of extracellular matrix (ECM) gel flanked by both side channels seeded with HUVEC followed by the 72 h treatment of 100 $\mu\text{g}\cdot\text{mL}^{-1}$ MC/5-FU (Fig. 9a). This model was designed based on previous reports to mimic the tumour-vasculature-drug interaction upon drug delivery (Nashimoto et al., 2020; Tsai et al., 2017). The growth of the spheroid based on the size difference was measured and compared over the 72 h treatment of MC/5-FU (Fig. 9b). From the microscopic examination, 100 $\mu\text{g}\cdot\text{mL}^{-1}$ MC/5-FU (IC_{50} on HCT116 spheroid) modestly inhibited the growth of spheroid compared to the untreated spheroid. The spheroid growth analysis showed about 5–10% inhibition in the MC/5-FU-treated spheroid over the course of 72 h treatment. As seen in Fig. 9d, the live/dead cell staining also showed modestly increased population of PI-stained dead cells in the MC/5-FU-treated spheroids while the population of healthy cells was comparable in both MC/5-FU-treated and untreated spheroid. Consistent with previous study (Kessel et al., 2017), bright green fluorescence was seen in the circumference of spheroids, indicating the proportion of actively proliferating healthy cells while the less intense fluorescence in the center of spheroids suggests the necrotic core.

The percent inhibition in the microfluidic co-culture model did not reach 50% as expected due to the more stringent tumour microenvironment which might have prevented the effective delivery of the drug. Similar finding has been previously reported when the hypoxia-inducible factor (HIF) inhibitor, YC-1 showed reduced anticancer activity in the osteosarcoma-derived microfluidic 3D spheroids which demonstrated the increased level of a cytokine — vascular endothelial growth factor (VEGF-A) (Sarkar et al., 2020).

3.17. Effect of magnetic targeting and temperature on HCT116 tumour spheroid killing

To evaluate the proof-of-concept of tumour targeting by super-magnetic MC/5-FU, an external magnet was used to direct the drugs towards the tumour spheroids on the microfluidic chip (Fig. 9c). However, no apparent anticancer enhancement was observed in the MC/5-

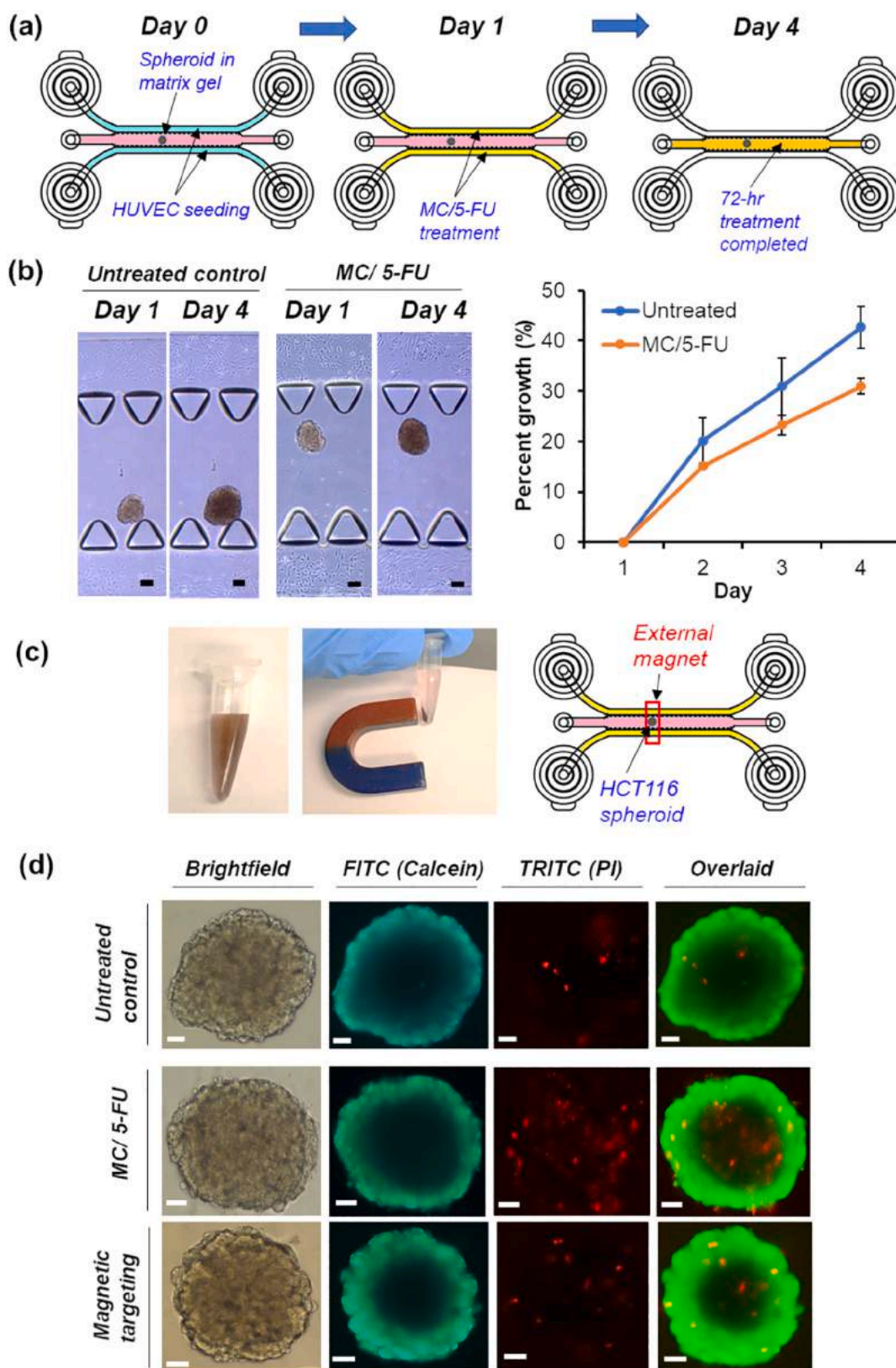


Fig. 9. Tumour spheroid-on-chip testing with MC/5-FU. (a) Schematic diagram showing the design of tumour spheroid-on-chip co-culture model with MC/5-FU treatment. (b) Microscopic examination (left) and spheroid growth analysis (right) of HCT116 spheroids treated with 100 $\mu\text{g}\cdot\text{mL}^{-1}$ MC/5-FU in comparison with untreated control. Scale bars represent 100 μm . (c) Magnetic property of MC/5-FU separated by external magnet (left) and schematic diagram showing the magnetic targeting towards tumour spheroid (right). (d) Calcein AM (live cells) and propidium iodide (dead cells) staining of untreated, MC/5-FU-treated spheroids with and without magnetic targeting. Scale bar represents 50 μm .

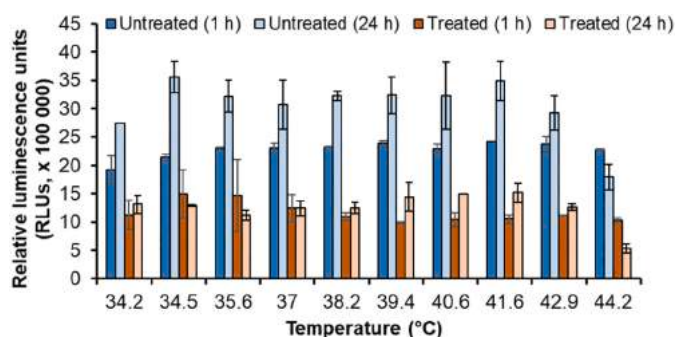


Fig. 10. Effect of short-term temperature induction on tumour spheroid killing. Tumour spheroids were exposed to 1 h temperature induction from 34.2 to 44.2 °C and the anticancer action of MC/5-FU was determined after 1 h and 24 h incubation.

FU-treated spheroids with and without magnetic targeting (Fig. 9d). This was evidenced by the comparable populations of both viable and dead cells as shown in the Calcein/PI staining.

Next, to assess the effect of hyperthermia treatment on the anticancer killing of MC/5-FU, a temperature gradient protocol was established using a thermal cycler. In Fig. 10, the relative luminescence units (RLUs) are proportional to the proliferating cell number. Consistent inhibition of MC/5-FU on the HCT116 spheroids from 34.2 to 44.2 °C after 1 h and 24 h incubation was consistently seen but no apparent enhancement of killing was seen at any specific temperature. Compared to the untreated spheroids, the MC/5-FU-treated spheroids failed to proliferate from 34.2 to 38.2 °C while only slight increase of growth was seen from 39.4 to 42.9 °C. Incubation at 44.2 °C was detrimental to the growth in both untreated and MC/5-FU-treated spheroids as seen in the reduced RLUs after 24 h incubation.

4. Conclusion

In summary, 5-FU-loaded magnetic rice straw cellulose (MC/5-FU) was developed to study its physicochemical properties, multi-stimuli responsive release of drug, and potential killing effects on colorectal cancer cells. The delignification, bleaching, and alkali treatments on rice straw waste degraded the amorphous region and liberated the crystal region of cellulose. Fe₃O₄-NPs were supported on cellulose by co-precipitation method, and then 5-FU was loaded onto the magnetic cellulose bionanocomposites. XRD, FTIR, XPS, and EDX analysis showed the successful synthesis of MC/5-FU as a multifunctional bionanocomposites. The SEM and TEM images revealed that the cellulose displayed a role as a matrix for Fe₃O₄-NPs as fillers. The bionanocomposites exhibited colloidal and thermal stability and saturation magnetization of 34.82 emu·g⁻¹. The effective 5-FU loading onto the MC carrier was estimated to be 62.50 ± 0.8%. The swelling ratio and 5-FU release from MC/5-FU increased with increase of pH and the temperature induction. MC/5-FU showed modest anticancer action in both 2D and 3D tumour spheroid models but reduced activity was seen in the tumour microenvironment-mimicking microfluidic co-culture model. From the caspase assay, MC/5-FU triggered apoptosis in the colorectal cancer cells. Mitochondrial membrane potential assay indicated that MC/5-FU affected the mitochondrial function to a very low extent. Furthermore, both MC and MC/5-FU showed insignificant toxicity to the red blood cells in hemolysis assay. Therefore, MC/5-FU could be a potential drug carrier candidate for its multifunctional physicochemical properties and anticancer effects. Further modification of the MC bionanocomposites is warranted to improve its anticancer activity in more stringent co-culture and *in vivo* models.

CRedit authorship contribution statement

Mostafa Yusefi: Conceptualization, Investigation, Methodology, Formal analysis, Writing – original draft, Validation, Software, Data curation. **Michiele Soon Lee-Kiun:** Investigation, Methodology, Formal analysis, Writing – original draft. **Kamyar Shameli:** Supervision, Conceptualization, Investigation, Methodology, Formal analysis, Writing – review & editing, Validation, Data curation. **Sin-Yeang Teow:** Supervision, Conceptualization, Investigation, Methodology, Formal analysis, Writing – review & editing, Validation, Data curation. **Roshafima Rasit Ali:** Writing – review & editing, Validation. **Kit-Kim Siew:** Investigation, Formal analysis, Software. **Hui-Yin Chan:** Investigation, Formal analysis, Software, Writing – review & editing. **Magdelyn Mei-Theng Wong:** Investigation, Conceptualization, Writing – review & editing. **Wei-Ling Lim:** Formal analysis, Writing – review & editing. **Kamil Kuća:** Writing – review & editing.

Declaration of competing interest

The authors report no declarations of interest.

Acknowledgment

This research was funded by Takasago Thermal Engineering Co. Ltd. grant (R.K.130000.7343.4B422) and Fundamental Research Grant Scheme (R.K130000.7843.5F403) from the research management center (RMC) of Universiti Teknologi Malaysia (UTM) and Malaysia Japan International Institute of Technology (MJIT). This work was also supported by Sunway University Internal Grant 2020 (GRTIN-RSF-SHMS-DMS-03-2020) and University of Hradec Kralove Excellence project (PrF UHK 2011/2021-2022).

References

- Anirudhan, T. S., Nima, J., & Divya, P. L. (2015). Synthesis, characterization and *in vitro* cytotoxicity analysis of a novel cellulose based drug carrier for the controlled delivery of 5-fluorouracil, an anticancer drug. *Applied Surface Science*, 355, 64–73.
- Bae, J., & Park, J. W. (2015). Preparation of an injectable depot system for long-term delivery of alendronate and evaluation of its anti-osteoporotic effect in an ovariectomized rat model. *International Journal of Pharmaceutics*, 480(1–2), 37–47.
- Bahrami, B., Behzad, T., Zamani, A., Heidarian, P., & Nasri-Nasrabadi, B. (2018). Optimal design of ozone bleaching parameters to approach cellulose nanofibers extraction from sugarcane bagasse fibers. *Journal of Polymers and the Environment*, 26(10), 4085–4094.
- Banerjee, A., Pathak, S., Subramaniam, V. D., Dharanivasan, G., Murugesan, R., & Verma, R. S. (2017). Strategies for targeted drug delivery in treatment of colon cancer: Current trends and future perspectives. *Drug Discovery Today*, 22(8), 1224–1232.
- Basta, A., Fierro, V., El-Saied, H., & Celzard, A. (2009). 2-Steps koh activation of rice straw: An efficient method for preparing high-performance activated carbons. *Bioresource Technology*, 100(17), 3941–3947.
- Bhandari, J., Mishra, H., Mishra, P. K., Wimmer, R., Ahmad, F. J., & Talegaonkar, S. (2017). Cellulose nanofiber aerogel as a promising biomaterial for customized oral drug delivery. *International Journal of Nanomedicine*, 12, 2021.
- Chen, X., Yu, J., Zhang, Z., & Lu, C. (2011). Study on structure and thermal stability properties of cellulose fibers from rice straw. *Carbohydrate Polymers*, 85(1), 245–250.
- Doane, T., & Burda, C. (2013). Nanoparticle mediated non-covalent drug delivery. *Advanced Drug Delivery Reviews*, 65(5), 607–621.
- Dolan, E. B., Haugh, M. G., Voisin, M. C., Tallon, D., & McNamara, L. M. (2015). Thermally induced osteocyte damage initiates a remodelling signaling cascade. *PLoS One*, 10(3), Article e0119652.
- Ebadi, M., Saifullah, B., Buskaran, K., Hussein, M. Z., & Fakurazi, S. (2019). Synthesis and properties of magnetic nanotheranostics coated with polyethylene glycol/5-fluorouracil/layered double hydroxide. *International Journal of Nanomedicine*, 14, 6661.
- Evans, B. A., Bausch, M. D., Sienerth, K. D., & Davern, M. J. (2018). Non-monotonicity in the influence of nanoparticle concentration on sar in magnetic nanoparticle hyperthermia. *Journal of Magnetism and Magnetic Materials*, 465, 559–565.
- Gupta, A., Tiwari, G., Tiwari, R., Srivastava, R., & Rai, A. (2015). Enteric coated hpmc capsules plugged with 5-fu loaded microsponges: A potential approach for treatment of colon cancer. *Brazilian Journal of Pharmaceutical Sciences*, 51(3), 591–605.
- Illangakoon, U. E., Yu, D.-G., Ahmad, B. S., Chatterton, N. P., & Williams, G. R. (2015). 5-Fluorouracil loaded eudragit fibers prepared by electrospinning. *International Journal of Pharmaceutics*, 495(2), 895–902.
- Ismail, N. A., Shameli, K., Wong, M. M.-T., Teow, S.-Y., Chew, J., & Sukri, S. N. A. M. (2019). Antibacterial and cytotoxic effect of honey mediated copper nanoparticles

- synthesized using ultrasonic assistance. *Materials Science and Engineering C*, 104, Article 109899.
- Izadiyan, Z., Shamel, K., Miyake, M., Hara, H., Mohamad, S. E. B., Kalantari, K., et al. (2020). Cytotoxicity assay of plant-mediated synthesized iron oxide nanoparticles using juglans regia green husk extract. *Arabian Journal of Chemistry*, 13(1), 2011–2023.
- Jiang, F., & Hsieh, Y.-L. (2013). Chemically and mechanically isolated nanocellulose and their self-assembled structures. *Carbohydrate Polymers*, 95(1), 32–40.
- Kadam, A., Saratale, R. G., Shinde, S., Yang, J., Hwang, K., Mistry, B., et al. (2019). Adsorptive remediation of cobalt oxide nanoparticles by magnetized α -cellulose fibers from waste paper biomass. *Bioresource Technology*, 273, 386–393.
- Kadry, G. (2019). Comparison between gelatin/carboxymethyl cellulose and gelatin/carboxymethyl nanocellulose in tramadol drug loaded capsule. *Heliyon*, 5(9), Article e02404.
- Kessel, S., Cribbes, S., Déry, O., Kuksin, D., Sincoff, E., Qiu, J., & Chan, L. L.-Y. (2017). High-throughput 3d tumor spheroid screening method for cancer drug discovery using celigo image cytometry. *SLAS Technology: Translating Life Sciences Innovation*, 22(4), 454–465.
- Khalid, A. M., Hossain, M., Ismail, N., Khalil, N. A., Balakrishnan, V., Zulkifli, M., & Yahaya, A. N. A. (2021). Isolation and characterization of magnetic oil palm empty fruits bunch cellulose nanofiber composite as a bio-sorbent for Cu (II) and Cr (VI) removal. *Polymers*, 13(1), 112.
- Lee, K. X., Shamel, K., Mohamad, S. E., Yew, Y. P., Isa, M., Dayana, E., et al. (2019). Bio-mediated synthesis and characterisation of silver nanocarrier, and its potent anticancer action. *Nanomaterials*, 9(10), 1423.
- Lesiak, B., Rangam, N., Jiricek, P., Gordeev, L., Tóth, J., Kóvér, L., et al. (2019). Surface study of Fe₃O₄ nanoparticles functionalized with biocompatible adsorbent molecules. *Frontiers in Chemistry*, 7, 642.
- Li, P., Yang, Z., Wang, Y., Peng, Z., Li, S., Kong, L., & Wang, Q. (2015). Microencapsulation of coupled folate and chitosan nanoparticles for targeted delivery of combination drugs to colon. *Journal of Microencapsulation*, 32(1), 40–45.
- Li, Y., Pang, H., Guo, Z., Lin, L., Dong, Y., Li, G., & Wu, C. (2014). Interactions between drugs and polymers influencing hot melt extrusion. *Journal of Pharmacy and Pharmacology*, 66(2), 148–166.
- Liao, J., & Huang, H. (2020). Review on magnetic natural polymer constructed hydrogels as vehicles for drug delivery. *Biomacromolecules*, 21(7), 2574–2594.
- Lu, P., & Hsieh, Y.-L. (2012). Preparation and characterization of cellulose nanocrystals from rice straw. *Carbohydrate Polymers*, 87(1), 564–573.
- Lu, Q., Zhang, Y., Hu, H., Wang, W., Huang, Z., Chen, D., et al. (2019). In situ synthesis of a stable Fe₃O₄@cellulose nanocomposite for efficient catalytic degradation of methylene blue. *Nanomaterials*, 9(2), 275.
- Nashimoto, Y., Okada, R., Hanada, S., Arima, Y., Nishiyama, K., Miura, T., & Yokokawa, R. (2020). Vascularized cancer on a chip: The effect of perfusion on growth and drug delivery of tumor spheroid. *Biomaterials*, 229, 119547.
- Nasri, S., Ebrahimi-Hosseinzadeh, B., Rahaie, M., Hatamian-Zarmi, A., & Sahraeian, R. (2020). Thymoquinone-loaded ethosome with breast cancer potential: Optimization, in vitro and biological assessment. *Journal of Nanostructure in Chemistry*, 10(1), 19–31.
- Niedzwiecki, D., Hasson, R. M., Lenz, H. J., Ye, C., Redston, M., Ogino, S., et al. (2017). A study of thymidylate synthase expression as a biomarker for resectable colon cancer: Alliance (cancer and leukemia group B) 9581 and 89803. *The Oncologist*, 22(1), 107.
- Nypelö, T., Rodriguez-Abreu, C., Rivas, J., Dickey, M. D., & Rojas, O. J. (2014). Magneto-responsive hybrid materials based on cellulose nanocrystals. *Cellulose*, 21(4), 2557–2566.
- de Oliveira, J. P., Bruni, G. P., Lima, K. O., El Halal, S. L. M., da Rosa, G. S., Dias, A. R. G., & da Rosa Zavareze, E. (2017). Cellulose fibers extracted from rice and oat husks and their application in hydrogel. *Food Chemistry*, 221, 153–160.
- Panja, S., Maji, S., Maiti, T. K., & Chattopadhyay, S. (2015). A smart magnetically active nanovehicle for on-demand targeted drug delivery: Where Van der Waals force balances the magnetic interaction. *ACS Applied Materials & Interfaces*, 7(43), 24229–24241.
- Pawlik, A., Nowak, J. M., Grzanka, D., Gackowska, L., Michalkiewicz, J., & Grzanka, A. (2013). Hyperthermia induces cytoskeletal alterations and mitotic catastrophe in p53-deficient h1299 lung cancer cells. *Acta Histochemica*, 115(1), 8–15.
- Pineda, X., Quintana, G. C., Herrera, A. P., & Sánchez, J. H. (2020). Preparation and characterization of magnetic cellulose fibers modified with cobalt ferrite nanoparticles. *Materials Chemistry and Physics*, 259(3), Article 122778.
- Sabaqian, S., Nemati, F., Nahzomi, H. T., & Heravi, M. M. (2017). Palladium acetate supported on amidoxime-functionalized magnetic cellulose: Synthesis, DFT study and application in Suzuki reaction. *Carbohydrate Polymers*, 177, 165–177.
- Sarkar, S., Peng, C.-C., & Tung, Y.-C. (2020). Comparison of VEGF-A secretion from tumor cells under cellular stresses in conventional monolayer culture and microfluidic three-dimensional spheroid models. *Plos One*, 15(11), Article e0240833.
- Seabra, A. B., Bernardes, J. S., Fávoro, W. J., Paula, A. J., & Durán, N. (2018). Cellulose nanocrystals as carriers in medicine and their toxicities: A review. *Carbohydrate Polymers*, 181, 514–527.
- Srasri, K., Thongroj, M., Chajjiraaree, P., Thiangtham, S., Manuspiya, H., Pisitsak, P., & Ummartyotin, S. (2018). Recovery potential of cellulose fiber from newspaper waste: An approach on magnetic cellulose aerogel for dye adsorption material. *International Journal of Biological Macromolecules*, 119, 662–668.
- Strassburg, S., Mayer, K., & Scheibel, T. (2020). Functionalization of biopolymer fibers with magnetic nanoparticles. *Physical Sciences Reviews*, 1, 1–27.
- Sukri, S. N. A. M., Shamel, K., Wong, M. M.-T., Teow, S.-Y., Chew, J., & Ismail, N. A. (2019). Cytotoxicity and antibacterial activities of plant-mediated synthesized zinc oxide (ZnO) nanoparticles using Punica granatum (pomegranate) fruit peels extract. *Journal of Molecular Structure*, 1189, 57–65.
- Sun, B., Zhang, M., Shen, J., He, Z., Fatehi, P., & Ni, Y. (2019). Applications of cellulose-based materials in sustained drug delivery systems. *Current Medicinal Chemistry*, 26(14), 2485–2501.
- Tan, T. H., Lee, H. V., Dabdawb, W. A. Y., & Abd Hamid, S. B. B. O. (2019). A review of nanocellulose in the drug-delivery system. In *Materials for biomedical engineering* (pp. 131–164). Elsevier.
- Teow, S.-Y., & Atif Ali, S. (2016). Antibacterial activity of a peptide derived from HIV-1 MN strain gp41 envelope glycoprotein against methicillin-resistant Staphylococcus aureus. *Pakistan Journal of Pharmaceutical Sciences*, 29(6).
- Teow, S.-Y., Liew, K., Mat, M. F. C., Marzuki, M., Aziz, N. A., Chu, T.-L., et al. (2019). Development of a luciferase/luciferin cell proliferation (XenoLuc) assay for real-time measurements of Gfp-Luc2-modified cells in a co-culture system. *BMC Biotechnology*, 19(1), 1–11.
- Tibolla, H., Pellissari, F. M., Rodrigues, M. I., & Menegalli, F. C. (2017). Cellulose nanofibers produced from banana peel by enzymatic treatment: Study of process conditions. *Industrial Crops and Products*, 95, 664–674.
- Todea, M., Muresan-Pop, M., Simon, S., Moisescu-Goia, C., Simon, V., & Eniu, D. (2018). Xps investigation of new solid forms of 5-fluorouracil with piperazine. *Journal of Molecular Structure*, 1165, 120–125.
- Tsai, H.-F., Trubelja, A., Shen, A. Q., & Bao, G. (2017). Tumour-on-a-chip: Microfluidic models of tumour morphology, growth and microenvironment. *Journal of the Royal Society Interface*, 14(131), 20170137.
- Wang, X., Liu, Y., Arandiyan, H., Yang, H., Bai, L., Mujtaba, J., et al. (2016). Uniform Fe₃O₄ microflowers hierarchical structures assembled with porous nanoplates as superior anode materials for lithium-ion batteries. *Applied Surface Science*, 389, 240–246.
- Xu, H., Aguilar, Z. P., Yang, L., Kuang, M., Duan, H., Xiong, Y., et al. (2011). Antibody conjugated magnetic iron oxide nanoparticles for cancer cell separation in fresh whole blood. *Biomaterials*, 32(36), 9758–9765.
- Xue, W., Liu, X.-L., Ma, H., Xie, W., Huang, S., Wen, H., et al. (2018). AMF responsive DOX-loaded magnetic microspheres: Transmembrane drug release mechanism and multimodality postsurgical treatment of breast cancer. *Journal of Materials Chemistry B*, 6(15), 2289–2303.
- Yew, Y. P., Shamel, K., Mohamad, S. E. B., Nagao, Y., Teow, S.-Y., Lee, K. X., & Isa, E. D. M. (2019). Potential anticancer activity of protocatechuic acid loaded in montmorillonite/Fe₃O₄ nanocomposites stabilized by seaweed Kappaphycus alvarezii. *International Journal of Pharmaceutics*, 572, Article 118743.
- Yusefi, M., Bte Rasit Ali, R., Abdullah, E. C., & Shamel, K. (2020). Analysis on physicochemical properties of cellulose fiber from rice straw waste. *MS&E*, 808(1), Article 012038.
- Yusefi, M., & Shamel, K. (2021). Nanocellulose as a vehicle for drug delivery and efficiency of anticancer activity: A short-review. *Journal of Research in Nanoscience and Nanotechnology*, 1(1), 30–43.
- Yusefi, M., Shamel, K., Ali, R. R., Pang, S.-W., & Teow, S.-Y. (2020). Evaluating anticancer activity of plant-mediated synthesized iron oxide nanoparticles using punica granatum fruit peel extract. *Journal of Molecular Structure*, 1204, Article 127539.
- Yusefi, M., Shamel, K., Hedayatnasab, Z., Teow, S.-Y., Ismail, U. N., Azlan, C. A., & Ali, R. R. (2021a). Green synthesis of Fe₃O₄ nanoparticles for hyperthermia, magnetic resonance imaging and 5-fluorouracil carrier in potential colorectal cancer treatment. *Research on Chemical Intermediates*, 1–20.
- Yusefi, M., Shamel, K., Jahangirian, H., Teow, S.-Y., Umakoshi, H., Saleh, B., et al. (2020). The potential anticancer activity of 5-fluorouracil loaded in cellulose fibers isolated from rice straw. *International Journal of Nanomedicine*, 15, 5417–5432.
- Yusefi, M., Shamel, K., Yee, O. S., Teow, S.-Y., Hedayatnasab, Z., Jahangirian, H., et al. (2021b). Green synthesis of Fe₃O₄ nanoparticles stabilized by a Garcinia mangostana fruit peel extract for hyperthermia and anticancer activities. *International Journal of Nanomedicine*, 16, 2515.
- Zhu, K., Ye, T., Liu, J., Peng, Z., Xu, S., Lei, J., & Li, B. (2013). Nanogels fabricated by lysozyme and sodium carboxymethyl cellulose for 5-fluorouracil controlled release. *International Journal of Pharmaceutics*, 441(1–2), 721–727.